Indian Journal of Pure & Applied Physics
Vol. 60, August 2022, pp. 662-679
DOI: 10.56042/ijpap.v60i8.63474

Vibrational Spectral Investigations, Hybrid Computational Analysis, Hirshfeld Surface and Molecular Docking Studies of 3-Hydroxy-4-Nitrobenzaldehyde

K Parimala[a]* & S Manimegalai[a]

[a]PG & Research Department of Physics, Nehru Memorial College (Affiliated to Bharathidasan University), Trichy-621 007, India

Received 24 May 2022; accepted 14 July 2022

As part of this study, the vibrational properties of 3H4NB were examined. Comparing observed and simulated vibrational spectra allowed for the identification of characteristic frequencies and the attribution of band names. For the density functional theory (DFT) calculations, the LSDA functional with 6-311++G(d,p) degree of approximation was used. Furthermore, the same level of theory was used to calculate molecular orbitals such as natural bond orbitals (NBOs) and the HOMO-LUMO energy gap. The condensed Fukui function and the molecular electrostatic potential (MEP) surface were used to determine the relative electrophilicity and nucleophilicity of the current molecule. Intermolecular hydrogen bonding interactions are studied using Hirshfeld surface analysis and fingerprint plots. Molecular docking analysis was used to investigate the compound's biological activities. The hydrogen bond active binding residues and binding energy of a chosen chemical with carcinogenic activity targets were examined.

Keywords: DFT; LSDA; MEP; NBO; Hirshfeld surface

1 Introduction

Intriguingly, the phenolic structure of 3-Hydroxy-4-nitrobenzaldehyde (3H4NB) is simple, consisting of two hydroxyl (donor) groups and a carbonyl (acceptor) group on benzene rings. A noncentrosymmetric crystal structure is formed when a chemical has a nitro group (NO2), which generally produces nonlinearity.

Antispasmodic activity can be discovered in phenolic compounds originating from plants, such as benzaldehyde and benzyl alcohol, and some of them, such piperonal, have it to a greater level and could be regarded suitable candidates[1]. Isovanillin, a phenolic aldehyde group found in many plants[2–5], inhibits aldehyde oxidase and is converted to isovanillic acid by aldehyde dehydrogenase[6,7]. The pharmacological effects of isovanillin on gastrointestinal function have not been studied, despite several investigations on the vanillin isomer.

There are naturally occurring chemical molecules that are similar in structure to vanillin (acetovanillon). Various plants were used to make it, and researchers are now looking at its extensive pharmacological qualities. In order to combat edoema and heart disease, the vanillin molecule is employed[8].

The vibrational spectrum analysis of 3H4NB has yet to be documented in quantum chemical calculations. Quantum chemistry calculations and HOMO–LUMO energies, as well as natural bond orbital analyses and vibrational assignments are all part of this project. A potential energy distribution (PED) of internal coordinates that correspond to covalent bonds was used for FT-IR and FT-Raman peak assignments in this study. Gaussian 09 software was used to calculate the molecule's quantum descriptors, including total energy, electron density distribution in the highest occupied molecular orbital (HUMO) and lowest unoccupied molecular orbital (LUMO), charge distribution, electronegativity (χ), absolute hardness (η), softness (σ), electrophilicity (χ), chemical potential (μ), and charge transfer in molecules (N_{max}).

The natural bond orbital (NBO) analysis was done with the same degree of basis functional to determine whether or not 3H4NB had intermolecular and intramolecular charge transfer interactions. TD-DFT and Gauge-Independent Atomic Orbital (GIAO) techniques were used to compute the absorption wavelengths and NMR chemical shifts, respectively. To further understand the active sites of retinol, the molecular electrostatic potential (MEP) surface was displayed across the optimised shape. Understanding the mechanism and biological activity of the title chemical against anticancer protein targets is accomplished using molecular docking. QTAIM, which offers electron density of atoms in terms of critical points, was utilised to investigate non-covalent interactions.

*Corresponding authors: (Email: kparimala79@yahoo.co.in)

2 Characterization Techniques

Lancaster Chemical Company offers solid 3-Hydroxy-4-nitrobenzealdehyde (3H4NB) with a purity claim of 98 percent. FT-IR and FT-Raman spectra could not be recorded using this method. The FT-IR spectra was acquired with a KBr pellet method with a resolution of 1.0 cm^{-1} on a PERKIN ELMER spectrophotometer equipped with mercury, cadmium, and tellurium detectors in the wavenumber region 4000–400 cm^{-1}. The ‘‘BRUKER RFS27’ ‘spectrophotometer fitted with a Raman module accessory running at 1.5 W power with the Nd: YAG laser's excitation wavelength of 1064 nm is used to record Raman scattering at room temperature.

A UV-Visible spectrophotometer using DMSO as a solvent was used to get the molecule's UV-Vis spectrum in the 800–100 nm wavelength range. In order to obtain nuclear magnetic resonance (NMR) spectra of 13C (CDCl3) and 1H (CDCl3), an instrument called the Bruker HC 400 was utilised. It is depicted in parts per million (scale) how tetramethylsilane's chemical composition of protons changes (TMS).

3 Computational Details

The implementation of computational study often provides supportive evidence to the experimental results. In this work, density functional theory calculations were performed using Gaussian 09 program package[9] at the LSDA/6-311++G(d,p) approximation levels of theory to find optimum energy structure, intramolecular charge transfer properties, vibrational harmonic frequencies, absorption wavelengths and NMR chemical shifts. For visualizing Cartesian coordinate displacements of vibrational modes and isodensity surfaces, the Gauss view 5.0 interface program was used[10]. The vibrational spectral assignments of FT-IR and FT-Raman peaks were done with the aid of the MOLVIB program package[11]. To find the isotropic chemical shift values of 1H and 13C NMR spectra, the Gauge-Independent Atomic Orbital (GIAO) method was employed[12]. The natural bond orbital (NBO) analysis[13] the NBO 3.1 interface programme of the Gaussian 09W package was used to detect intramolecular delocalization and hyper conjugative interactions using the DFT approach with the combined basis set LSDA/6-311++G(d,p). The QTAIM (quantum topological atoms in molecules) programme used to find the intramolecular interactions[14]. To validate the results obtained from AIM analysis, the multi-wave function analysis was performed by Multiwfn software[15]. The molecular electrostatic potential (MEP) surfaces of the retinol were plotted in order to investigate the retinol's reactive sites (electrophilic and nucleophilic). In addition, Auto Dock 4.2 software was used to undertake molecular docking analyses of 3H4NB with a variety of anti-cancer protein targets[16].

4 Result and Discussion

4.1. Conformational analysis

In quantum chemical computations, potential setups are utilised to identify the lowest-energy molecule geometry (global minimum). Fig. 1 depicts the four potential configurations a–d. LSDA/6-311++G(d,p) calculations were used to compute the total energies and energy differences (the relative energy of the other conformers was as: “b” is the lowest energy as a reference point) for all conformers of 3H4NB, and they are shown in Table 1. The conformer “b” has the lowest global energy, and as a result, it was chosen for further computations since it is the most stable conformer. As

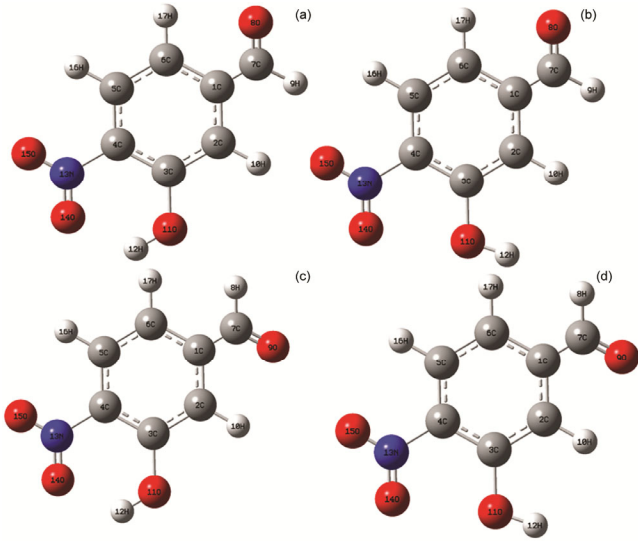

Fig. 1 — Stable conformers C1, C2, C3 and C4 of 3H4NB.

Table 1 — Calculated energies and energy differences for two conformers of 3H4NB using LSDA methods with 6-311++G(d,p) basis set.

Conformers	Energy (Hartree)	Energy ($kJmol^{-1}$)	differences* ($kJmol^{-1}$)
a	–395.8908	–1039411.775	3.10975
b	–395.8929*	–1039456.888	0.00000
c	–395.8918	–1039423.812	3.10999
d	–395.8911	–1039438.759	3.10992

*Global minimum energy

indicated in Table 1, the conformers "c" were found to be the least stable, according to the computations. The conformer "b" is projected to be more stable from 3.10975, 3.10999, and 3.10992 kJ/mol than the other conformers in the 6-311++G(d,p) basis set.

4.2. Optimized geometry

Fig. 2 depicts 3H4NB's optimized structures and atom numbering. Table 2 includes a summary of the most optimal structural characteristics, as well as experimental evidence to back them up. In Table 2, geometrical parameters including bond lengths, bond angles, and dihedral angles were compared to experimental values for the 3H4NB structure, which was optimised at the LSDA level of functional.[17]. As seen in Fig. 2, the 3H4NB molecule contains aromatic hydrocarbons connected by an unsaturated CC linear chain, as well as three chemically active functional groups (OH, CHO, and NO2). At LSDA with 6-311++G(d,p) basis set, the O1–H51 bond distance is predicted to be 0.9633 based on the bond length of a hydroxyl group. Because of the influence of substitutions, the estimated bond lengths of aromatic C–C atoms such C1–C2, C2–C3, C3–C4, C4–C5, C5–C6 and C6–C7 are shorter than the experimentally

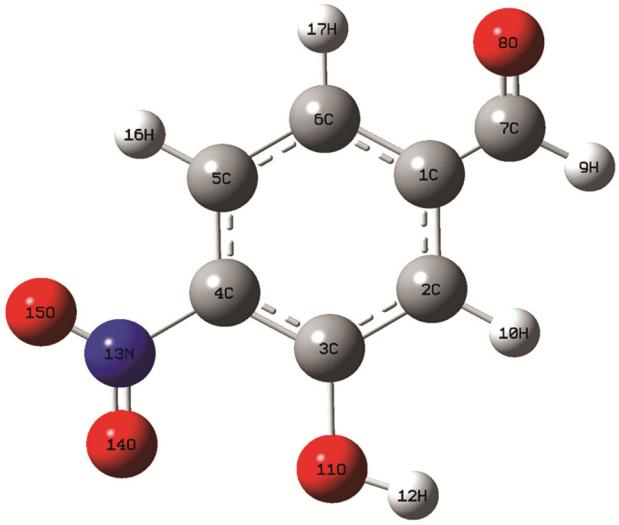

Fig. 2 — Optimized Molecular structure of 3H4NB along with numbering of atoms.

Table 2 — Optimized geometrical parameters of 3H4NB bond lengths (Å), angles (º) and dihedral angles (º) by LSDA/6-311++G(d,p) method.

Lengths	Values (Å)	Exp[a]	Angles	Values (º)	Exp[a]	Dihedral angles	Values (º)	Exp[a]
C1–C2	1.3952	1.403	C2–C1–C6	119.9985	119.4	C6–C1–C2–C3	0.0323	−2.0
C1–C6	1.3948	1.385	C2– C1–C7	119.9972	120.3	C6–C1–C2–H10	129.9532	119.997
C1–C7	1.3996	1.473	C6–C1–C7	120.0043	120.4	C7–C1–C2–C3	–179.9729	178.5
C2–C3	1.3947	1.370	C1–C2–C3	120.0086	121.1	C7–C1–C2–H10	–0.052	
C2–H10	1.0997	0.950	C1–C2–H10	119.9808	119.5	C2–C1–C6–C5	0.0149	2.1
C3–C4	1.3954	1.408	C3–C2–H10	120.0106	119.7	C2–C1–C6–H17	179.9892	
C3–O11	1.3473	1.341	C2–C3–C4	119.9942	120.6	C7–C1–C6–C5	–179.9798	−178.3
C4–C5	1.3948	1.399	C2–C3–O11	120.0128	115.9	C7–C1–C6–H17	–0.0056	
C4–N13	1.4358	1.457	C4–C3–O11	119.993	126.4	C2–C1–C7–O8	–139.0531	0.2
C5–C6	1.3951	1.394	C3–C4–C5	119.994	117.7	C2–C1–C7–H9	40.9469	
C5–H16	1.0998	0.950	C3–C4–N13	119.9811	121.1	C6–C1–C7–O8	40.9416	−179.5
C6–H17	1.0996	0.950	C5–C4–N13	120.0249	117.1	C6–C1–C7–H9	–139.0584	
C7–O8	0.9612	1.222	C4–C5–C6	120.0047	121.8	C1–C2–C3–C4	–0.0568	1.9
C7–H9	0.6923	0.950	C4–C5–H16	120.0113	119.5	C1–C2–C3–O11	179.9619	−178.7
O11–H12	1.0254	0.845	C6–C5–H16	119.984	119.7	H10–C2–C3–C4	–179.9777	
N13–O14	0.9672	1.242	C1–C6–C5	120.0	119.4	C2–C3–C4–C5	0.041	1.9
N13–O15	0.9647	1.223	C1–C6–H17	120.008	120.3	C2–C3–C4–N13	0.0341	−1.6
			C5–C6–H17	119.992	120.3	O11–C3–C4–C5	–179.9964	179.0
			C1–C7–O8	120.0	122.4	O11–C3–C4–N13	–179.9846	177.8
			C1–C7–H9	120.0	118.8	C2–C3–O11–H12	–0.0151	
			O8–C7–H9	120.0	118.8	C4–C3–O11–H12	3.9541	
			C3–O11–H12	109.4712	106.1	C3–C4–C5–C6	–176.0272	−176.03
			C4–N13–O14	120.0	118.1	C3–C4–C5–H16	0.0131	
			C4–N13–O15	120.0	119.0	N13–C4–C5–C6	–179.9995	−179.8
			O14–N13–O15	120.0	122.8	N13–C4–C5–H16	–179.9563	
						C3–C4–N13–O14	–3.3939	−169.8
						C3–C4–N13–O15	176.6061	−170.0
						C5–C4–N13–O14	176.5755	−171.0

[a]Ref. [17].

measured bond distances. When substituents with electron-withdrawing properties are added to the rings, the symmetry of the ring is disrupted, causing bond length variations at the point of substitution. The aldehyde group is to blame for the NLO effect of the molecule's name.

C2–H10, C5–H16, and C6–H17 have bond lengths of 1.0997, 1.0998, and 1.0996, respectively. Because of the repulsive effect present in the H10, H16, and H17 atoms, the experimental values (0.950) of the three O–H bond values are virtually comparable. The length of the C–H bond in the ring of an aldehyde is greater, whereas the length of the C–H bond is shorter. Distorsions in hybridization may be traced back to substituent effects on carbons where they are connected. A shift in bond angle values at the substitution site causes the phenyl ring's off-kilter hexagonal symmetry.

The exocyclic bond angles C2–C1–C6 (119.9985º), C1–C2–C3 (120.0086º), C2–C3–C4 (119.9942º), C3–C4–C5 (119.994º), C4–C5–C6 (120.0047º) and C1–C6–C5 (120.0º) for 3H4NB molecule. The C2–C1–C6, C2–C3–C4 and C3–C4–C5 values were slightly deviated from the standard value 120 °in which the substitution is nitro group, hydroxyl group and the aldehyde group in place of O, N and H atoms.

4.3. Vibrational frequency analysis

In the present work, the spectral and spectroscopic description of 3H4NB has been examined using the both experimental and theoretical FT-IR and FT-Raman spectrum. 3H4NB consists of 17 atoms, which possesses 45 normal modes of vibration. Potential energy distribution (PED) was estimated for each normal mode together with the symmetry coordinates. The entire vibrational assignments of fundamental modes of 3H4NB together with the PED are shown in Table 3. The computed IR intensities (Km mol^{-1}), Raman intensities (Å4amu^{-1}), Reduced masses (amu), force constants (m dyneÅ^{-1}), depolarization ratios (polarised (P) and polarised (U)) are derived for 3H4NB using LSDA technique with 6-311+G(d,p) basis set presented in Table 4. The actual and theoretical FT-IR and FT-Raman plots are illustrated in Figs. 3 and 4 respectively.

4.3.1 O–H Vibrations

The single hydroxyl (OH) group in the title molecule 3H4NB generates three vibrations, *i.e.* (stretching, in-plane and out-of-plane bending vibrations). This is the most sensitive group, with noticeable changes in the spectra of the hydrogen bound assembly in response to changes in the environment. In general[18], O−H stretching vibrations appear in the region 3400–3500 cm^{-1}. The O–H in-plane bending vibration ranges between 1250 and 1150 cm^{-1}. At 1309 cm^{-1}, the estimated wavenumbers are in good agreement with the actual values of 1309 cm^{-1} in this 3H4NB, and the O–H in-plane bending vibration is clearly visible in the FT-IR and FT-Raman spectra.

In general[19], The OH in-plane bending vibration ranges between 1250 and 1150 cm^{-1}. At 1309 cm^{-1}, the estimated wavenumbers are in good agreement with the actual values of 1309 cm^{-1} in this 3H4NB, and the O−H in-plane bending vibration is clearly visible in the FT-IR and FT-Raman spectra. O−H out-of-plane bending vibration lies[20] in the region 710−517 cm^{-1}. The theoretically computed wave number is predicted at 742 cm^{-1}.

4.3.2 C–H Vibrations

Aromatic compounds typically have a C–H stretching vibration of 3100–3000 cm^{-1} 3H4NB has a C–H stretching vibration at 3400(vs) and 3320(w) cm^{-1} in the FT-IR spectrum. The theoretically values were estimated at 3269, 3115 and 2984 cm^{-1}. The C–H in-plane ring bending vibrations[22] was found in the 1300–1000 cm^{-1} and 950–800 cm^{-1} ranges. Medium and very weak bands at 1480, 1250, and 1070 cm^{-1} in the FT-IR spectrum were found for the C–H in-plane bending vibrations whereas strong and extremely strong bands at 1480 and 1250 cm^{-1} in the FT-Raman spectrum were discovered. The C–H out-of- plane bending vibrations occur[23] around 900–667 cm^{-1}. At 872 cm^{-1} and 829 cm^{-1} in the infrared, and in the Raman spectrum, the C–H out-of-plane bending vibrations may be seen.

4.3.3 C–C Vibrations

Stretching modes are predicted in the range of 1650–1200 cm^{-1}. As allocated by this study, the peaks in the FT-IR spectra at 1461 cm^{-1} and 1437 cm^{-1} in FT-Raman correspond to CC ring vibrations and are in good agreement with values determined by LSDA/6-311++G(d,p) using a different approach. Vibrational modes at 584, 635 and 679 cm^{-1} in FT-Raman are ascribed to CC in-plane bending, which corresponds to the experimental wave numbers, and the wave numbers are consistent. Table 3 shows the computed values for the compound's out-of-plane bending peaks at 569 and 703 cm^{-1} in FT-IR and FT-Raman spectra.

Table 3 — Comparison of the observed and calculated vibrations of 3H4NB by LSDA levels with 6-311++G(d,p) basis set.

Mode	FT-IR	FT-Raman	Unscaled	Scaled	PED≥10%
1	3560(w)		3589	3456	νOH(98)
2	3400(vs)		3361	3269	νCH(95)
3	3320(w)		3190	3115	νCH(94)
4			3078	2984	νCH(92)
5		2840(w)	2915	2883	νCH(C=O)(88)
6	2450(s)	2620(vw)	2756	2529	νCC(83)
7	2240(s)		1953	2018	νC=O(81)
8	1560(vw)	1580(s)	1645	1574	NO2 asym(85)
9		1500(m)	1588	1468	NO2 sym (74)
10	1480(m)	1480(s)	1509	1398	βCH(63)+βOH(27)+βCN(42)
11	1400(vw)	1415(w)	1418	1309	βOH(92)+ NO2 rock(65)+νCC(43)
12		1320(vw)	1348	1284	βCH(C=O)(47)+βCC(27)+βC=O(15)
13	1250(m)	1250(vs)	1294	1261	βCH(52)+βCN(26)+ βCC41)
14		1240(m)	1259	1232	νCC(54)+γOH(41) + νCN(18)
15		1200(vs)	1224	1209	νCC(57)+νCH(34)+βCN(22)
16	1100(w)	1100(w)	1167	1121	νCC(69)+νCH(33)+νCO(23)
17	1070(vw)		1076	1017	βCH(58)+βOH(27)+βCN(12)
18	1050(vw)	1000(m)	1040	998	νCC(52)+νOH(28)
19		850(vw)	961	945	νCC(56)+νOH(25)+ NO2 rock(12)
20		830(w)	912	892	νCN(44)+ NO2 sym(31)+ NO2 wagg(17)
21		790(s)	906	845	νCC(57)+νCO(34)+βCN(22)
22			829	803	γCH(49)+βCO(27)+βCN(15)
23			761	742	γOH(45)+βCH(35)+βCN(22)
24		700(w)	706	661	γCH(51)+βCO(29)+βCN(11)
25	600(vw)	630(vw)	674	624	NO2 sciss(54)+νCC(57)+νCN(15)
26		580(m)	596	572	γCH(49)+βCO(26)+βCN(14)
27			552	521	νCO(OH)(62)+νCC(36)
28		500(vw)	538	498	NO2 rock(63)+νCC(32)+ NO2 sym(17)
29		480(vw)	476	453	NO2 wagg(49)+Rasymd(47)+νC=O(24)
30	400(w)		450	425	γCH(C=O)(47)+βCC(27)+βC=O(15)
31			378	352	βsymd(58)+ NO2 sciss(22)+νCN(15)
32			351	332	βC=O(48)+Rtrigd(38)+νCN(34)
33			341	325	NO2 twist(36)+γCN(12)
34			322	308	βasymd(41)+βCN(22)+βC=O(12)
35		300(vw)	305	283	βRtridg(41)+γCH(31)+γCN(18)
36			292	265	βCC(45)+βCN(30)+βOH(17)
37			274	236	tRasymd(59)+opr(33)+γCN(14)
38			243	209	βCN(49)+ NO2 sciss(32)+βC=O(11)
39		220(vw)	213	196	tRsymd(39)+γCC(20)+γOH(13)
40		180(w)	183	174	γCN(39)+ NO2 twist(30)+βCH(12)
41			165	161	γC=O(41)+Rtrigd(27)+νCN(14)
42			132	125	βCO(OH)(32)+γCN(26)+γOH(13)
43			117	105	tRtridg(36)+γCH(24)+γCN(17)
44		100(m)	100	93	γCC(35)+γCN(24)+γC=O(18)
45			85	65	γCO(OH)(33)+γCC(12)

Experimental relative intensities are abbreviated as follows: vs-very strong, s-strong, m-medium, w-weak, w-very weak. asym-asymmetric stretching, sym-symmetric stretching, β-in-plane bending, γ-out-of-plane bending, sciss-scissoring, rock-rocking, wagg-wagging, twist-twisting, R-ring, trigd-trigonal deformation, symd-symmetric deformation, asymd-asymmetric deformation, t-torsion.

4.3.4. Aldehyde group vibrations

Among the three stretching vibrations that the aldehyde group produces are C=O (C=H) and C–C (C=C). C=O stretching and C–H stretching are the most essential of the three aldehyde group stretchings. Aldehyde C–H stretching absorption usually appears as two medium-intensity bands at 2850–2720 cm^{-1}. C–H stretching in the aldehyde group was ascribed to the existence of an FT-Raman band with a wavelength of 2840(w) cm^{-1}. The theoretical values for 3H4NB were determined to be 2883 cm1 in the experiment. Aldehyde[25] C–H bending vibration which appears around 1400 cm^{-1}. It was determined that the 1320(vw) cm^{-1} bands in the FT-Raman spectrum were caused by C–H bending vibration. There is a very strong and distinct band that appears at 1700 cm^{-1} in

Table 4 — IR intensities (Km mol^{-1}), Raman intensities ($Å^4amu^{-1}$), Reduced masses (amu), force constants (m dyne$Å^{-1}$), depolarization ratios (polarized (P) and polarized (U)) are obtained for 3H4NB calculated by LSDA method with 6-311+G(d,p) basis set.

No.	IR intensities	Raman intensities	Reduced masses	Force constants	Depolarization ratios	
					P	U
1	88.97	64.84	2.12	1.21	0.84	0.86
2	98.54	72.53	1.08	1.16	0.34	0.41
3	433.18	95.93	1.06	1.14	0.23	0.25
4	4.17	68.77	2.11	1.21	0.79	0.83
5	2.16	75.75	3.12	1.12	0.85	0.87
6	2.08	99.63	1.04	2.23	0.13	0.08
7	589.33	35.57	7.52	8.67	0.57	0.65
8	527.15	4.98	6.83	5.83	0.39	0.42
9	148.36	9.96	4.74	4.74	0.79	0.83
10	137.84	8.56	5.45	6.48	0.27	0.18
11	83.21	14.04	3.52	3.52	0.36	0.41
12	9.08	9.35	3.53	4.53	0.26	0.42
13	27.14	8.33	2.05	2.07	0.74	0.86
14	2.15	14.45	2.92	5.93	0.45	0.65
15	22.77	0.53	3.07	2.07	0.51	0.68
16	27.09	6.24	1.35	3.35	0.36	0.56
17	228.68	7.45	1.83	1.83	0.08	0.15
18	32.54	2.14	3.67	4.69	0.45	0.67
19	21.66	3.17	2.17	3.17	0.29	0.48
20	34.34	4.14	4.14	4.14	0.17	0.27
21	4.76	1.15	1.15	0.15	0.74	0.84
22	34.85	3.03	3.67	2.67	0.18	0.38
23	25.09	0.34	4.68	1.65	0.75	0.86
24	29.87	1.11	12.74	10.74	0.76	0.87
25	8.88	1.43	9.38	9.32	0.77	0.88
26	5.54	12.69	6.34	6.34	0.18	0.27
27	4.63	25.67	7.63	5.65	0.07	0.14
28	34.77	0.88	3.65	2.63	0.74	0.88
29	28.05	2.27	4.29	3.27	0.53	0.68
30	74.67	1.39	2.18	1.16	0.77	0.86
31	23.66	2.08	7.12	6.14	0.65	0.79
32	24.35	1.09	2.14	1.13	0.76	0.84
33	3.23	6.04	5.47	4.47	0.45	0.66
34	3.29	2.15	3.83	2.83	0.72	0.83
35	2.67	1.16	1.26	0.26	0.76	0.84
36	5.78	3.57	6.83	5.84	0.17	0.35
37	1.05	1.26	1.25	0.25	0.74	0.87
38	7.07	0.45	4.96	3.96	0.76	0.86
39	0.45	1.47	7.57	7.57	0.77	0.84
40	11.66	1.04	2.15	1.12	0.75	0.87
41	176.94	2.18	3.14	1.13	0.79	0.86
42	29.27	3.65	6.56	5.54	0.75	0.84
43	24.36	2.06	2.27	1.27	0.76	0.85
44	21.54	3.22	5.97	4.97	0.77	0.88
45	11.25	4.67	8.58	7.55	0.75	0.85

the C=O stretching band[26]. The C=O stretching in aldehyde group is clearly seen in the FT-IR spectra at 2240 cm^{-1}. A C=O bond's computed value for 2018 title compounds. The vibration of the aldehyde group shows that this molecule has NLO action.

4.3.5. NO_2 Vibrations

Aromatic nitro compounds have strong absorptions due to the asymmetric and symmetric stretching vibrations of the NO2 group at 1570–1500 cm^{-1} and 1370–1300 cm^{-1}, respectively[27, 28]. Hydrogen bonding has a little effect on the NO2 asymmetric stretching vibrations[29]. According to the PED findings, the NO2 asymmetric and symmetric stretching for the title molecule is allocated to modes 8 and 9. Asymmetric vibration has been ascribed to the spectra at 1560(vw) in the FT-IR and 1580(s) in the FT-Raman of the title

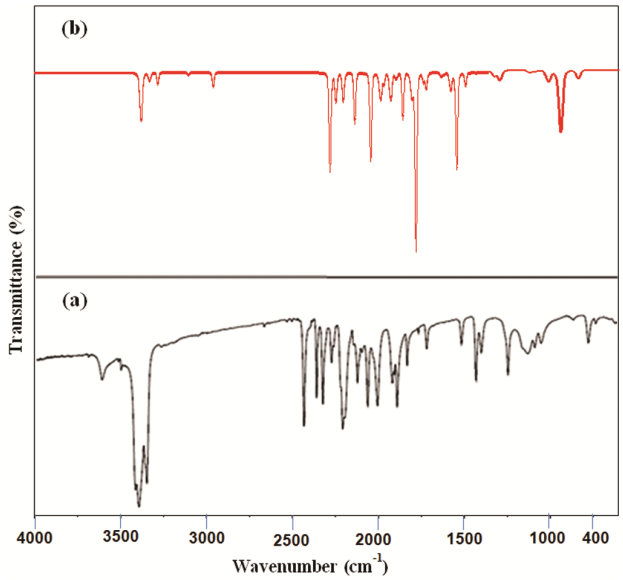

Fig. 3 — Simulated FT-IR spectra of 3H4NB (a) observed, (b) calculated by LSDA/6-311++G (d,p).

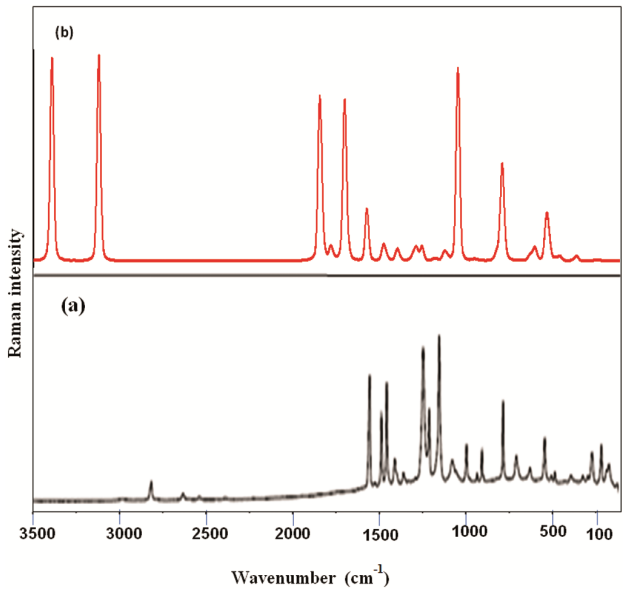

Fig. 4 Simulated FT-Raman spectra of 3H4NB (a) observed and (b) calculated by LSDA/6- 311++G (d,p).

molecule, whereas symmetric vibration has been assigned to the spectra at 1500(m) cm1 in the FT-Raman. For asymmetric stretching, the PED of these modes contributes 85% of the time and 74% for symmetric stretching. Low-frequency normal modes are influenced by the NO2 group's other vibrations, such as scissoring, rocking, wagging, and twisting. To explain why aromatic nitro compounds exhibit a band of weak to medium intensity in the 590–500 cm^{-1} range, we need to understand how the NO2 group

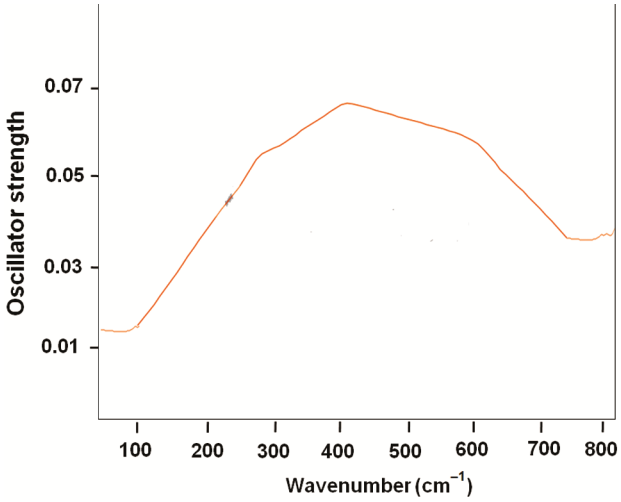

Fig. 5 — Experimental UV-vis spectrum for 3H4NB in water solvent.

bends out of plane (wagging and twisting)[30]. The wagging vibration is observed at 480(vw) cm^{-1} in FT-Raman spectrum (calculated 453 and 325 cm^{-1}). Likewise, the in-plane (scissoring and rocking) NO2 deformation vibrations[31, 32] have a week to medium absorption in the region 775–660 cm^{-1}. Vibration at 600(vw) cm^{-1} is detected in the FT-IR spectrum, and 630(vw) cm^{-1} is anticipated in the FT-Raman spectrum, and the computed scissoring vibration is 624 cm^{-1} using the LSDA technique, in this instance. Vibration measured at 498 cm^{-1} in the FT-Raman spectrum of a rocking mode at 500(vw) cm^{-1}. To sum up, based on this assignment's literature review, it is obvious that its vibrational frequency remains unaffected.

5 Photo Optical Properties

TD-DFT/LSDA technique with 6-311++G(d,p) basis set was used to compute the oscillator strengths (f) of the 3H4NB in vacuum, DMSO, and water in order to determine experimental absorption wavelengths (in nm) and estimated absorption wavelengths (in nm). The experimental UV spectra of the title chemical is shown in Fig. 5, as well. The n→π*, π→π* and n→σ* transitions may be identified by the measured wavelengths (nm) of the title chemical at 600, 400, and 280 nm. Table 5 shows that the experimental and computed wavelength values of the title compound are in good agreement for the values at (exp/cal.) 600/621.18 (by vacuum), 400/465.65 (by vacuum), and 280/265.30 (by vacuum) nm, respectively.

Table 5 — The calculated absorption wavelength λ (nm), excitation energies E (eV) and oscillator strengths (*f*) of 3H4NB calculated by TD-DFT/LSDA/6-311++G(d,p) level of theory in vacuum and solvent (DMSO and water) phase.

Excitation level	Wavelength λ (nm)	LSDA/6-311++G(d,p)								
	Expt.	Vacuum			DMSO			Water		
		E (eV)	λ(nm)	(*f*)	E (eV)	λ(nm)	(*f*)	E (eV)	λ(nm)	(*f*)
H–2→L+1		3.745	631.41	0.035	3.747	631.71	0.038	3.741	631.41	0.035
H→L										
H–1→L	600	3.866	621.18	0.006	0.864	621.70	0.006	3.860	621.61	0.006
H→L+1		4.347	485.39	0.006	4.342	485.49	0.006	4.344	485.39	0.006
H→L+2										
H–1→L+1		4.485	476.57	0.004	4.476	476.98	0.004	4.482	476.57	0.003
H–3→L	400	4.669	465.65	0.005	4.659	466.08	0.005	4.667	465.68	0.004
H–1→L+2										
H–4→L	280	4.857	265.30	0.153	4.852	266.04	0.215	4.856	265.38	0.015
H–3→L										
H→L+1										
H→L+2										

Table 6 — The experimental and calculated ^{13}C and ^{1}H NMR isotropic chemical shifts (δ in ppm) of 3H4NB by LSDA/6-311++G(d,p) level of theory.

Atoms	δppm (Calculated)	Experimental	Atoms	δppm (Calculated)	Experimental
C1	83.08	80	H9	7.312	8.2
C2	124.65	130	H10	0.425	0.3
C3	139.09	142	H12	9.787	10.1
C4	157.62	156	H16	7.347	7.1
C5	43.75	40	H17	8.295	7.5
C6	133.06	122			
C7	193.48	192			

6 Carbon and Proton NMR Spectral Analysis

An internal standard, tetramethylsilane, was used as an internal standard for the 1H and 13C NMR spectra of the title chemical at 298 K. Table 6 shows the observed and estimated chemical shifts (values) for 1H and 13C nuclei, as well as Fig. 6. The DFT/LSDA technique with 6-311++G(d,p) level theory was used to make the GIAO calculations. A high degree of agreement was found between the predicted 1H and 13C chemical changes and the measured values. An aromatic benzene carbon's 13C NMR signal (ppm) ranges from 156–40 ppm in the title molecules and is determined to be 157–43.75 ppm using the LSDA technique. In the experiment, the aldehyde group's C7-atom-bound benzene ring is seen at 192 ppm, which is higher than the theoretical value of 193.48 ppm. Carbon atom C7 is shielded or deshielded by more electronegative oxygen atoms due to their withdrawing nature, which causes an NMR chemical shift at higher ppm. Carbon atoms in the benzene ring have 13C NMR chemical shifts that are downfielded. These results show that there is something different going on with the carbon of anhydrous group at C3 (139 ppm) than there is at C2.

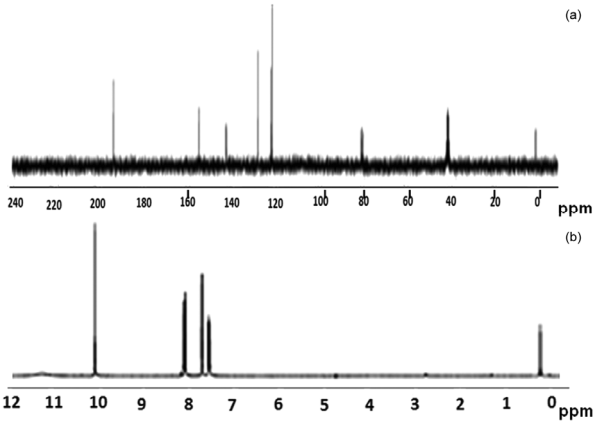

Fig. 6 — Experimental (a) 13C and (b) 1H NMR spectra of 3H4NB in CDCl3.

Proton para groups close to electron-withdrawing hydroxyl groups are deshielded, while aromatic protons ortho groups next to electron-donating groups are protected, as seen by the location of chemical shift values on a 1H NMR spectrum. There are isotropic chemical shifts in the range of 8.295–0.425 ppm, and potential peak values in the range of 7.5–0.3 ppm, for aromatic hydrogen atoms. The maximal signals for proton H17 are seen at 7.5 ppm and computed to be

8.295 ppm. The H10 atom in the benzene ring is detected at 0.3 ppm in a broad field. For the H12 atom in particular, its 1H chemical shift displays an upfield shift of 10.1 ppm because it is immediately connected to the more electronegative O. At 8.2 ppm, the other protons in H9 have a chemical shift that corresponds to the same signals that have been estimated to be at 7.312 ppm.

7 NLO Studies

It was confirmed that (I) had nonlinear optical property using the Kurtz and Perry technique[33] With modulated light at a wavelength of 1064 nm, a Nd:YAG laser was used to illuminate the powdered test material. The specimen was submitted to the SHG test with 1.2 mJ/pulse of radiation input. The powder SHG efficiency of (I) was found to be 8mV, which is two times larger than that of 3H4NB (4 mV) under the same circumstances (Table 7). NLO applications might benefit from this compound's high SHG efficiency.

For the specimen, we estimated the average polarizability α_0 (10^{-24} esu) and the anisotropy polarizability βtot (10^{-24} esu), the initial hyperpolarizability β_0 (10^{-24} esu), and electric dipole moment (Debye (D)) of the specimen are –30.739 $\times10^{-24}$ esu, 11.178 $\times10^{-24}$ esu, 4.678 $\times10^{-24}$ esu (~29 times of urea) and 3.596 D, respectively (Table 7). The electron cloud's delocalization is greater toward the x-axis, as seen in the table. Hyperconjugation, molecular symmetry, aromaticity, substitutability and charge transfer are some of the processes that are commonly associated with an elevated tot value in organic chemistry[34]. The nonlinearity and interactions between intra- and intermolecular hydrogen bonds. The dipole moment difference between the ground state and the first - electron excited state might also account for the high first-order molecule hyperpolarizability[35]. Because of the massive microscopic structures that result from this supramolecular assembly.

8 NBO Analysis

The LSDA technique with 6-311++G(d,p) level of theory, as provided in Gaussian 09W software, was used to investigate NBO calculations[9, 36]. In investigating inter- and intramolecular interactions between bonds, it is possible to employ both interactions in filled (donor) and empty (acceptor) orbitals as a method of research. In a molecular system, it may also be used to study conjugative interaction or charge transfer[37]. NBOs of the Lewis type (donor) and non-Lewis type (acceptor) are technically empty in an idealised Lewis structure image. Consequently, the Lewis structure's filled NBOs are ideally suited to depict covalent interactions in molecules. During the NBO study, all conceivable interactions between 'filled' (donor) Lewis-type NBOs and non-Lewis NBOs are examined, and then second-order perturbation theory is used to determine the energies of these interactions. Second-order perturbation interactions (E(2)) are used to quantify these interactions (or energetic stabilizations) known as 'delocalization' corrections to the zeroth-order natural Lewis structure[38]. This energy is used to estimate the off-diagonal NBO Fock matrix elements. The second-order perturbation method can be used to solve this problem[39]. Using equation (1).

$$E^{(2)} = q_i \frac{F(i,j)^2}{\varepsilon_j - \varepsilon_i} \quad \ldots (1)$$

Table 7 — The electric dipole moment μ (Debye), average polarizability α_0 ($\times10^{-24}$ esu), anisotropy polarizability βtot ($\times10^{-24}$ esu), initial hyperpolarizability β_0 ($\times10^{-24}$ esu) and vector hyperpolarizability βvec ($\times10^{-24}$ esu) for 3H4NB calculated by LSDA levels with 6-311++G(d,p) basis set.

Parameters	Moment values	Parameters	Moment values
μ_x	–2.578	β_{xxx}	–11.986
μ_y	–0.209	β_{xxy}	–4.142
μ_z	0.308	β_{xyy}	12.817
μ	3.596	β_{yyy}	–28.318
α_{xx}	–58.781	β_{xxz}	1.513
α_{xy}	4.596	β_{xyz}	0.079
α_{yy}	–65.212	β_{yyz}	0.897
α_{xz}	–0.107	β_{xzz}	24.379
α_{yz}	0.108	β_{yzz}	–2.945
α_{zz}	–72.847	β_{zzz}	0.745
α_0	–30.739	β_0	4.678
βtot	11.178	βvec	3.954

In this case, qi is the orbital occupancy and i and j are the diagonal elements. Lewis type NBOs and non-Lewis NBOs have the most critical interactions shown in Table 8 (donor/acceptor). As shown in Table 9, the results of NBO analysis show that in all four phases, the LP(3)O12 and LP(2)O13 bonding orbitals served as donors, while the *N10–O11 and *C2–C3 antibonding orbitals served as acceptors, resulting in stabilization energies of 160.60 and 30.55 kcal/mol and allowing intramolecular charge transfer and molecule stabilization. That's what we know for sure: The interaction between LP(3)O12/π*N10–O11 and LP(2)O13/ π*C2–C3 contributed considerably to the stabilization of the investigated molecule, as demonstrated by their high stabilization energy of 160.60 kcal/mol and 30.55 respectively. An additional factor that helped to keep this molecule in place was the contact between atoms of bond π*C2–C3/π*C1–C6, which had an energy of 272.19 kcal/mol.

9 Frontier Molecular Orbitals

The molecular reactivity and chemical stability of the molecule are determined by the frontier molecular orbitals. Frontier molecular orbitals include both the highest-occupied (HOMO) and lowest-unoccupied (LUMO) molecular orbitals. HOMO and LUMO both have the capacity to absorb and give electrons. EHOMO energy is proportional to the electron affinity (A = ELUMO), and this is also true for LUMO energy, which correlates to the ionisation potential (I = –EHOMO). Among molecular orbital theory, the π–π* transition is noticed as a result of the interaction between HOMO and LUMO orbitals[40]. By using the LSDA/6-311++G(d,p) approach, the HOMO, HOMO–1, and HOMO–2 border molecular orbitals (LUMO, LUMO+1, and LUMO+2) energies are estimated in the current work. Nodes of the HOMO and LUMO orbitals are represented by the colours red and green because of their positive and negative phases, respectively. Fig. 7 depicts the boundary molecular orbital positive and negative areas in visual form. The energy band gap E (difference in energy between the HOMO and LUMO orbital values) of the 3H4NB is determined to be 31.681 eV via LSDA theory. Large HOMO–LUMO energy gaps point to molecules with limited charge transfer that are more stable in complicated environments. Bonding orbitals stretch out among all carbons, and the higher-order orbital (HOMO) is above them. Oxygen atom on the surface of the HOMO has non-bonding orbital lobes although the ring and methyl groups of LUMO are positioned in the centre, they are not part of the LUMO molecular structure. It is important to note, however, that all three types of HOMO surfaces are concentrated on the rings and hydroxyl substitutions (HOMO–1 and HOMO–2). The aldehyde group has an orbital overlap with all the LUMO surfaces. The following parameters may be determined using the formulae below, which are based on HOMO and LUMO energy levels[41].

$$\text{Electronegativity } (\chi) = (I+A) / 2 \quad \ldots (2)$$

$$\text{Chemical potential } (\mu) = -((I+A)) / 2 \quad \ldots (3)$$

$$\text{Chemical hardness } (\eta) = (I-A) / 2 \quad \ldots (4)$$

$$\text{Chemical softness } (\sigma) = 1/2\ \eta \quad \ldots (5)$$

Table 8 — Selected NBO results showing formation of Lewis and non-Lewis orbitals for 3H4NB using LSDA/6-311++G(d,p) level of theory.

Bond (A–B)	ED/Energy(a.u)	ED_A (%)	ED_B (%)	NBO	S (%)	P (%)
σ(C7–O8)	1.984	29.87	72.14	$0.529(sp^{99.72})C+0.848(sp^{99.98})O$	01.81	99.72
					02.57	38.77
π(C7–O8)	1.981	39.98	63.02	$0.724(sp^{1.67})C+0.782(sp^{1.15})O$	38.65	63.38
					47.56	54.02
σ (C7–H9)	1.979	32.76	65.23	$0.672(sp^{2.33})C+0.817(sp^{0.89})H$	310.12	69.81
					54.01	47.87
σ(O11–H12)	1.976	47.54	53.44	$0.796(sp^{3.32})O+0.718(sp^{6.36})H$	24.23	77.72
					15.49	85.18
π(O11–H12)	1.978	54.23	47.74	$0.816(sp^{2.02})O+0.697(sp^{2.75})H$	34.24	66.76
					27.71	74.25
σ(N13–O14)	1.987	21.96	29.05	$0.849\ (sp^{2.77})N+0.526(sp^{0.01})O$	24.54	74.38
					98.97	05.02
π(N13–O15)	1.988	22.97	29.04	$0.849(sp^{2.76})N+0.525(sp^{0.01})O$	27.65	74.24
					99.97	04.02

Table 9 — Second order perturbation theory analysis of Fock matrix on NBO basis for 3H4NB using LSDA method With 6-311G++(d,p) basis set.

Donor NBO	Acceptor NBO (j)	[a]$E^{(2)}$ (Kcal/mol)	[b]E(i)-E(j) (a.u)	[c]F(i,j) (a.u)
σ(C7–O8)	σ*(C1–C2)	1.01	1.70	0.037
	σ*(C1–O8)	2.10	1.71	0.054
	σ*(C7–O8)	4.38	1.86	0.081
	σ*(C7–H9)	0.67	1.90	0.032
	σ*(C1–O8)	0.86	1.66	0.034
σ(C7–H9)	σ*(C1–C2)	4.51	1.08	0.062
	σ*(C1–C6)	3.66	1.04	0.056
	σ*(C5–C6)	0.37	0.27	0.013
	σ*(C5–C6)	114.97	1.24	0.488
σ(O11–H12)	σ*(C2–C3)	3.22	0.98	0.050
	σ*(C3–C4)	2.88	1.13	0.051
σ(N13–H14)	σ*(C3–C4)	11.89	1.10	0.103
	π*(C3–C4)	2.28	1.01	0.066
σ(N13–H15)	σ*(C3–C4)	0.94	1.68	0.051
	π*(C3–C4)	2.10	1.01	0.065
LP(O8)	σ*(C1–O8)	0.44	1.06	0.056
	σ*(C8–H9)	1.03	1.05	0.086
	σ*(C1–C2)	1.77	1.35	0.062
	σ*(C1–C6)	0.45	1.36	0.031
	σ*(C5–C6)	0.32	1.37	0.027
LP(O11)	σ*(C3–C4)	2.20	1.65	0.076
	π*(C3–C4)	1.64	0.96	0.056
	σ*(C2–C3)	3.73	1.40	0.091
LP(N13)	σ*(C3–C4)	1.96	1.33	0.065
	σ*(C4–C5)	4.82	1.34	0.101
	σ*(C5–C6)	0.34	1.32	0.027

[a]$E^{(2)}$ means energy of hyper conjugative interactions (stabilization energy). [b]Energy difference between donor and acceptor i and j NBO orbitals. [c]F(i,j) is the Fock matrix element between i and j NBO orbital.

Electrophilicity index (ω) =$\mu 2/2\eta$ … (6)

Maximum charge transfer index, $\Delta Nmax = (-\mu) / \eta$ … (7)

Where I and A are ionization potential and electron affinity; all these values are calculated and predicted in the Table 10.

10 Molecular Electrostatic Potential (MEP)

Fig. 8 depicts the MEP plot of the electrostatic potential mapped (LSDA/6-311++G(d,p)) on the constant electron density surface to demonstrate the distribution of the electrostatic potential. Because it concurrently represents molecule size, shape, dipole moment and electrostatic potential areas in terms of colour grading[42], MEP is important. Between –8.283e–2 and 8.283e–2 is the colour code for this map". The aldehyde and hydroxyl gropus cation is shown in blue and is surrounded by a positive electrostatic potential. The anion of the nitro group is coloured red because it has a lower electrostatic potential than the cation. Hydrogen bonding connections between the atoms in the red and blue sections are stronger than those in the other regions. Fig. 8 depicts the 3H4NB molecule.

11 Mulliken Population Analysis

Mulliken charges arise from the Mulliken population analysis[43] and provide a means of estimating partial atomic charges from calculations carried out by the methods of computational chemistry. Mulliken atomic charge distribution is displayed in Fig. 9. Electron donors are all the other oxygen atoms except for the deprotonated oxygen (O8), hydrogen-substituted carbons, and the nitro group nitrogen (N13). Calculations of mulliken atomic charges based on the basis function's definition of each atom's electron population are summarized in Table 11. There is a propensity for the most electropositive atoms like C7 to take an electron. C1 through C6 are negatively charged carbon atoms in the phenyl ring, whereas all of the hydrogen atoms are electropositive.

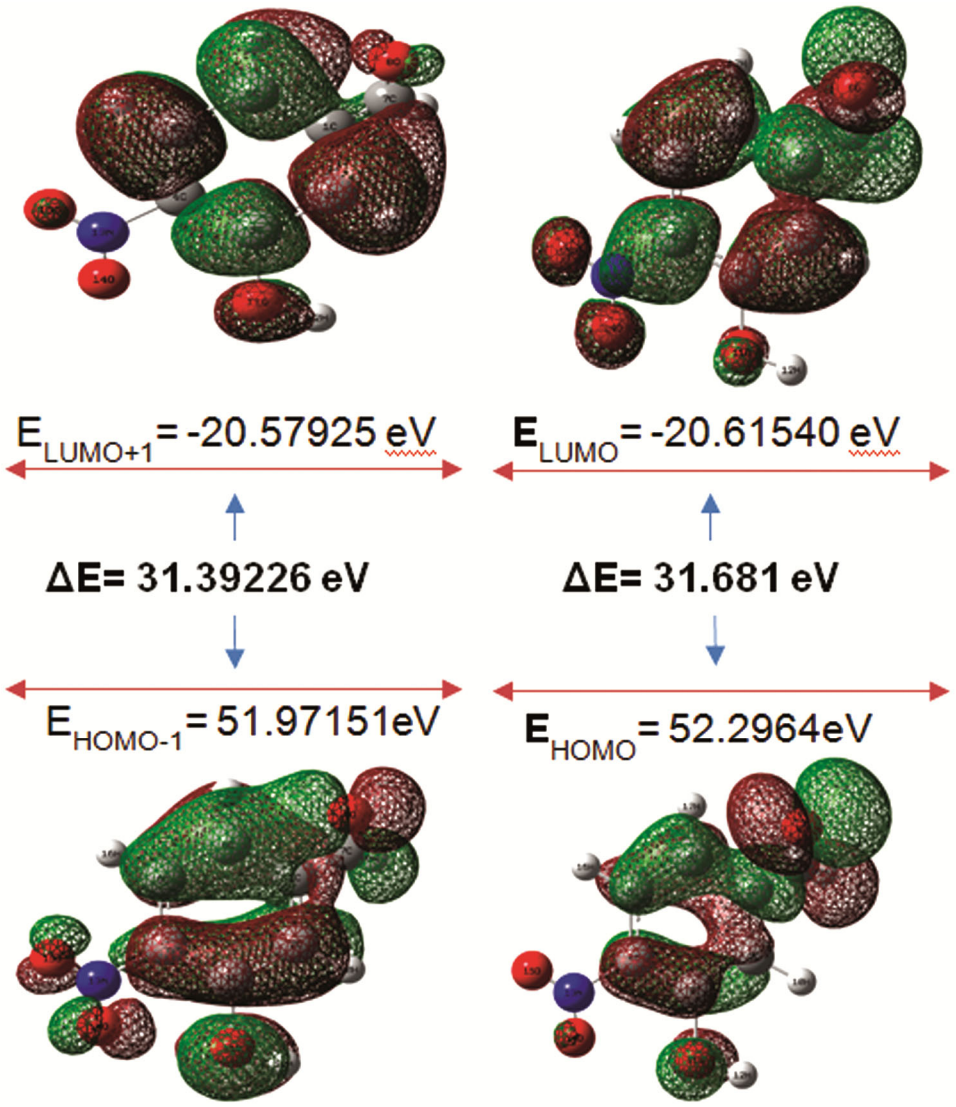

Fig. 7 —. Patterns of the principle highest occupied and lowest unoccupied molecular orbitals of 3H4NB obtained with LSDA/6-311++G(d,p) method in

Table 10 — Comparison of HOMO and LUMO energy gaps and related molecular properties of 3H4NB calculated by LSDA/6-311++G(d,p) method.

Molecular properties	Energy (eV)	Energy gap	Ionisation potential (I)	Electron affinity (A)	Global hardness (η)	Electro negativity (χ)	Global softness (σ)	Chemical potential (μ)	Global electrophilicity (ω)
HOMO	–0.324	0.056	0.323	–0.377	–0.353	0.027	0.353	–0.031	0.015
LUMO	0.381								
HOMO–1	–0.403	–0.365	0.405	–0.053	–0.227	–0.179	0.227	0.177	0.0347
LUMO+1	0.053								
HOMO–2	–0.421	–0.369	0.416	–0.054	0.237	0.185	–0.237	0.185	0.0394
LUMO+2	0.054								

12 Hirshfeld Surface Analysis

Molecule packing modes and hydrogen bonding interactions may be seen on the Hirshfeld surface. A graph was made showing the distance di to the closest atom within the surface and the distance de to the closest atom outside the surface. Fig. 10 depicts the 3H4NB's surface interactions in terms of dnorm, de, di and curvedness, with blue patches denoting shorter

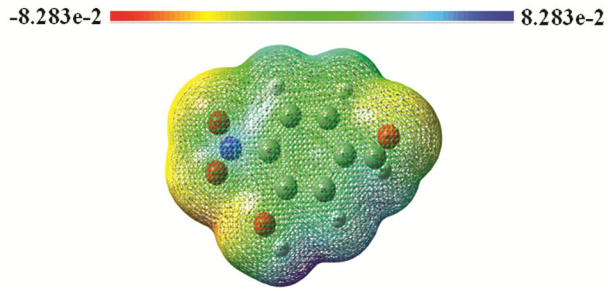

Fig. 8 — Electrostatic potential contour map of 3H4NB.

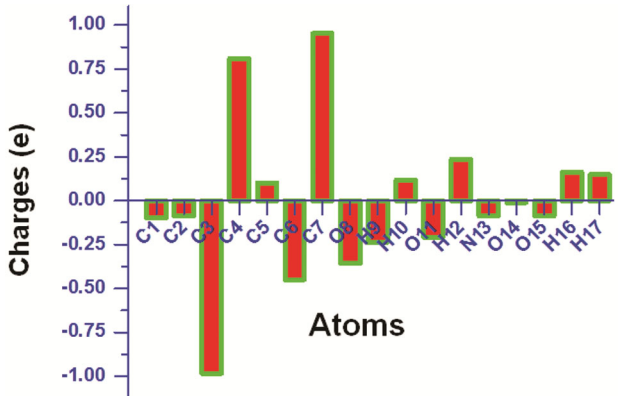

Fig. 9 — Comparative Mulliken plot by LSDA/6-311++G (d,p) level for 3H4NB.

Table 11 — Mulliken atomic charge of 3H4NB performed at LSDA method with 6-311++G(d,p) basis set.

Atoms	Atomic Charges
C1	–0.0982
C2	–0.0827
C3	–0.9827
C4	0.8095
C5	0.1007
C6	–0.4486
C7	0.9515
O8	–0.3577
H9	–0.2365
H10	0.1165
O11	–0.2075
H12	0.2359
N13	–0.0867
O14	–0.0107
O15	–0.0862
H16	0.1612
H17	0.1485

and longer intercontacts, respectively. Fig. 11 shows finger print plots on the contacts. C...C (14 percent), C...H (7.5 percent), C...O (2.4 percent), C...H (14.5 percent), H...O (14.5 percent), O...H (16.7 percent) and O...C (0.8 percent) are the most common types of contact identified on the Hirshfeld surfaces. Other

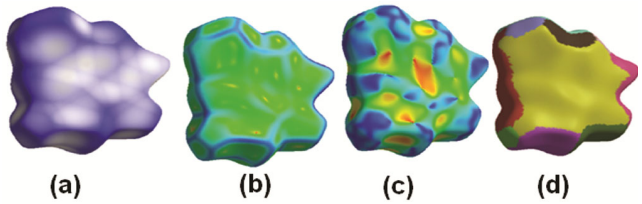

Fig. 10 — Hirshfeld surface graphical representation for 3H4NB molecule (a) dnorm (b) curvedness (c) shape index (d) fragement path

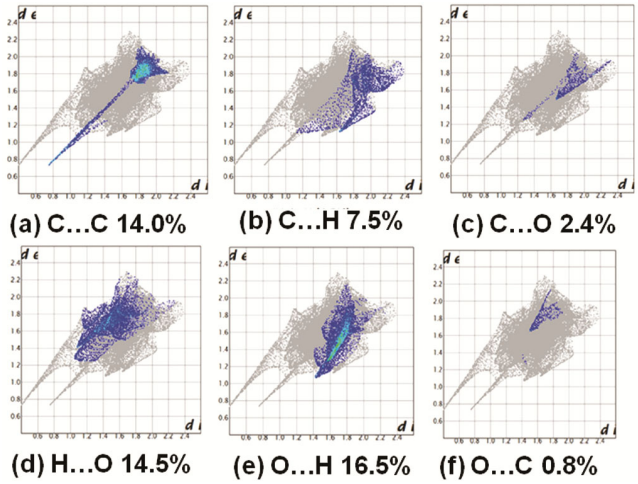

Fig. 11 — Graphical representation of the 2D Hirshfeld surface fingerprint plots for the interactions in the crystal structure of the 3H4NB molecule. a)C…C (b) C…H (c) C…O (d) H…O (e) O…H (f) O…C.

than hydrogen bonds, this surface map presented in the interaction of C...O/O...C shows weaker and longer contact in the lower extent red colour on the surface. The OH and CHO groups suggest strong and weak intermolecular interactions, as seen by these Hirshfeld surface 3D maps and 2D fingerprint plots.

13 Topology Analysis

13.1. Fukui Functions

The Fukui function and other electron density-based local reactivity descriptors have been created to shed light on a chemical framework's synthetic selectivity or reactivity at certain locations. A molecular structure's electron density is a data bank for all of its details. Parr and Yang[44] devised a limited approach for discriminating between figure Fukui function indices. Fukui function-condensed atoms in a molecular framework promote increased reactivity in the framework. Lee et al.[45] I've studied the condensed Fukui function and concluded that the chemical reaction's most responsive site has the higher f_k value.

For the uninitiated, Fukui indices are a type of reactivity index that reveal which atom's particles have a greater tendency to lose or accept electrons, and therefore, which atom's particles are more likely to experience a nucleophilic or electrophilic assault. Defintion: Fukui function[45]

$$F(r)=\left(\frac{\delta\rho(r)}{\delta N}\right)r \quad \ldots (8)$$

In this equation, (r) symbolises the electrical density, N represents the number of electrons, and r represents the nucleus' external potential. Because it displays the preferred locations where density changes occur when electron number changes, Fukui's work is a useful descriptor for studying how materials behave locally. After that, it is shown that the electrical density has the ability to distort at certain locations while receiving or supplying electrons[46, 47]. Likewise, it is possible to define the corresponding condensed or atomic Fukui functions on the k^{th} particle site as, for nucleophilic attack

$$f_k^+ = qk(N+1) - qk(N) \quad \ldots (9)$$

for electrophilic attack

$$f\bar{k} = q_k(N) - q_k(N-1) \quad \ldots (10)$$

for free radical attack

$$f_k^0 = 1/2[q_k(N+1) - q_k(N-1)] \quad \ldots (11)$$

Symbols such as + (nucleophilic), - (electrical), and - (radical) denote these three types of reactions. Anionic (N+1) and cationic (N–1) chemical species have the same atomic charge at the kth atomic site, qk, in these equations. An active site's pin point dispersion may be determined using the Fukui function. What it is worth is totally determined by the sort of charges that are applied to it. Recent work by Morell et al.[48] has set up a dual descriptor F(r), which is defined by the equation as the contrast between the nucleophilic and electrophilic Fukui functions,

$$\Delta F(r) = \left[f_k^+ - f\bar{k} \right] \quad \ldots (12)$$

Figure 12 depicts the electrophilic (Fj-) and nucleophilic (Fj+) sites. A nucleophilic attack is more likely when dual descriptor F(r) > 0, whereas an electrophilic attack is more likely when dual descriptor F(r) 0 is utilised. The title compound's anions and cations were studied in the current work using the ground state with doublet multiplicity and the optimised molecular geometry for single point DFT calculations. Mulliken population analysis (MPA) has been used to derive the Fukui function using the individual atomic charges.

In order to prevent the pattern from being broken by the reactive sites provided by the atomic descriptor. Stable structures of 3H4NB and related compounds have had their responsive sites computed. The most electrophilic sites in 3H4NB and similar compounds are at atoms H10 and C14. For nucleophilic assault, the most reactive sites are on N13 and H17, respectively. A dual descriptor F(r) value has shown that C1, C3, N13, O14, and O15 are vulnerable to nucleophilic assault, but the corresponding F(r) values for the other atoms in 3H4NB are less vulnerable to nucleophilic attack. Table 12 shows the electrophilic, nucleophilic, and

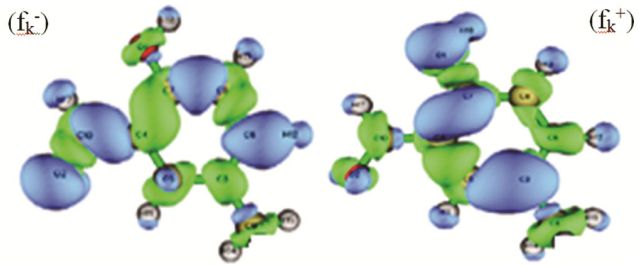

Fig. 12 — Plots of the RDG versus the electron density ρmultiplied by the sign of λ2 for 3H4NB.

Table 12 — Values of the Fukui function considering Mulliken charges according with equation (12–14) for 3H4NB obtained by LSDA level with 6-311++G(d,p) basis set.

Atoms	f_k^+	f_k^-	f_k^0
C1	**0.185**	**–0.217**	–0.018
C2	–0.227	0.244	–0.117
C3	**0.025**	**–0.226**	–0.093
C4	**0.426**	0.027	**0.226**
C5	–0.377	0.428	**0.028**
C6	**0.105**	**–0.376**	–0.237
C7	**0.567**	**–0.103**	**0.222**
O8	–0.009	0.566	**0.276**
H9	–0.458	0.007	–0.225
H10	**0.447**	**–0.458**	–0.007
O11	–0.127	0.249	**0.168**
H12	**0.033**	0.084	–0.043
N13	**0.815**	0.038	**0.429**
C14	**0.454**	**–0.459**	–0.008
C15	–0.135	0.247	**0.165**
H16	**0.026**	0.085	–0.046
H17	**0.817**	0.038	**0.429**

free radical values of 3H4NB and all of its related compounds. More electrophilic assault than nucleophilic or radical attack is contained in the title Analysis of Fukui functions and MEP and atomic charge values are in good agreement.

13.2. Reduced density gradient (RDG) analysis

An electron density (ED) and its derivatives may be utilised to expose the weak interactions, such as inter-molecular and even covalent interactions in real space, using the reduced density gradient (RDG).[49]. It is defined as

$$RDG(r) = \frac{1}{2(3\pi^2)^{1/3}} \frac{|\Delta\rho(r)|}{\rho(r)^{4/3}} \quad \ldots (13)$$

Where denotes the ED and (r) is the gradient vector's norm in terms of the ED. Mapping (r) versus sign 2 reveals information on the molecule's interactions, including their type and intensity. It was decided to use the 2 sign to distinguish between attracting and repulsive interactions that were either bound (2 0) or not. In order to better see the RDG vs the electron density, the sign of the 2 sign was added to the Fig. 13. The results were calculated by Multiwfn and VMD program[50, 51], respectively. Multiwfn's RDG analysis of the 3H4NB results in a visual depiction of non-covalent interactions and high repulsion. While green indicates Van der Waals interaction, dotted red hues suggest repulsive contacts (steric effect), and blue indicates attractive interactions (hydrogen bond) accordingly, RDG investigations were carried out to determine the nature of the molecule's interactions. Repulsive interactions have been found in the ring of the current compound, which indicates a significant steric influence in the molecule. Van der Waals interactions were found between the hydroxyl oxygen and the hydrogen atom of aldehyde. Van der Waals interactions between the ring hydrocarbon and the oxygen of the aldehyde were also seen. Molecule 3H4NB has strong attractive interactions, as seen by its blue coloration and its negative value of (2) (hydrogen bond). Intramolecular hydrogen bond interactions were observed between the oxygen hydroxyl and aldehyde hydrogen atoms (H12–O11...H9).

14 Molecular Docking

According to the findings in this study, docking analysis was used to determine how well 3H4NB ligands inhibit human serum albumin and the epidermal growth factor receptor (EGFR) while also increasing the isoform selectivity of their anti-cancer efficacy. Molecular docking is a typical method for figuring out how a small molecule medication interacts with macromolecules that don't have covalent bonds. Carbohydrates and proteins (bio-macromolecular targets) may be calculated using the Autodock tool. It can also be used to create new drugs. In the study of medicinal chemistry, such as chemical compounds, biological and pharmacological

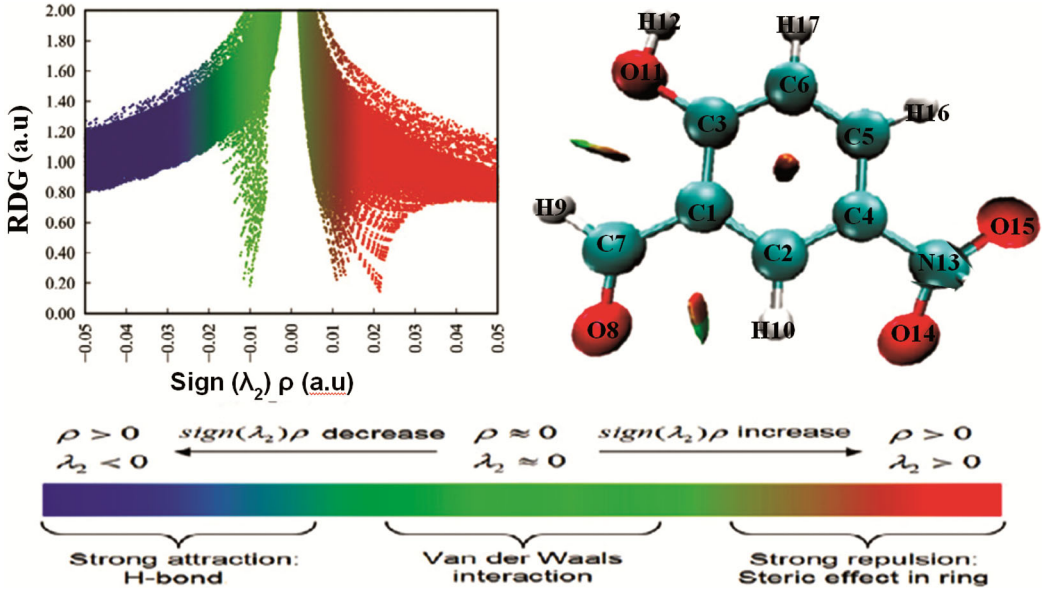

Fig. 13 — The binding configuration of 3H4NB and interaction analysis. Result of 2D interaction analysis shows hydrogen bond (green dashed lines) and hydrophobic interaction (red curved lines) using LigPlot.

qualities of synthetic analogues towards pathogens, quantitative structure activity relationships (QSAR) technique is used. With the Schrödinger Glide programme, the docking research was carried out with extreme precision (XP) (Maestro 12.7)[52,53]. Figs. 14 and 15 illustrate the best-scoring docking posture for the chemical (3H4NB), along with the key residues in the binding site. The molecule (3H4NB) with the lowest binding energy was identified through docking testing, and its value is –5.8. We discovered that the bulk of the ligands make hydrogen bonds with the residues Asp128, Asn130, Ser137, and Asp183, while they build hydrophobic contacts with His126 through docking tests. Slide molecular docking was used to identify which of these interactions had the lowest binding strength, as shown in Table 13 (PDB: 4ERT).

15 Thermo Molecular Characteristics

There are some important thermo molecular characteristics that have been found to be critical in material characterization and understanding of reactivity or mode of action as well as environmental influences on the mole. These include zero-point vibrational energy, enthalpy, Gibbs free energy, internal energy, heat capacity, thermal energy and partition functions (Fig. 16). The title chemical's thermodynamic properties are fascinating to examine in this study. Based on theoretical thermodynamic characteristics, vibration analysis was used to calculate Cp, enthalpy changes (H–E/T), entropy, and Gibbs free energy (G–E/T) for the title molecule. When utilised as a reactant in a new method, the thermodynamic values can be helpful in subsequent research on the title compounds. Tables 14 & 15 of 3H4NB list several thermodynamic properties that can be used to forecast a compound's chemical reactivity and stability. (G–E/T) drops as temperature rises, whereas all of the thermodynamic parameters measured rise (Fig. 16). There was greater evidence that the molecular thermodynamic system is more adaptable to temperature changes when looking at the H–E/T and S–entropy (S) fluctuations. Additionally, essential statistical variables with their fitted graphs have been included in the display. The following are the fitting equations for 3H4NB's thermal properties:

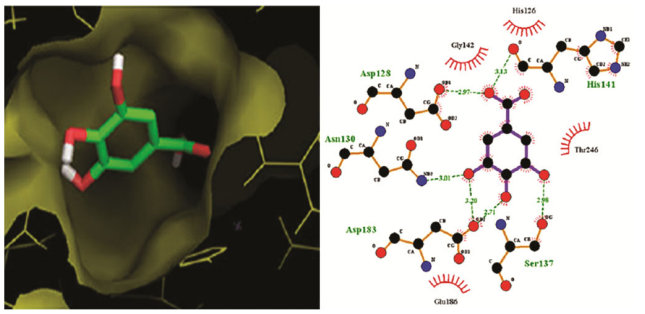

Fig. 14 — Three-dimensional graphical representations of the charged surfaces of most important ligand-protein complex with close view showing the enfolding of the ligand in the active site.

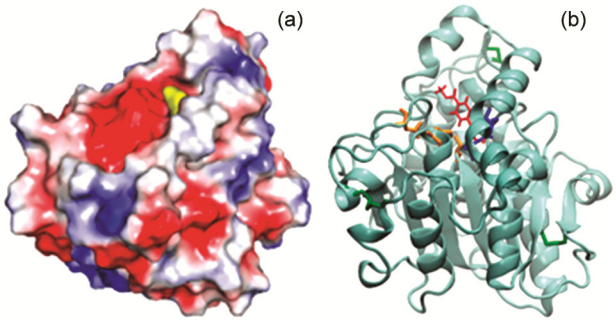

Fig. 15 — Ribbon model of the protein showing hydrogen bond with ligand as solid lines to 3H4MB.

Table 13 — Lowest binding energy for the ligand 3H4NB and ER protein (PDB: 4ERT).

Mode	Affinity	Dist from best mode	
	(kcal/mol)	rmsd l.b.	rmsd u.b.
1.	–5.8	0.000	0.000
2.	–5.4	1.478	4.220
3.	–5.3	1.225	4.313
4.	–5.3	1.776	4.395
5.	–4.8	19.556	20.971
6.	–4.5	20.108	20.993
7.	–4.5	18.943	20.276
8.	–4.4	17.913	19.457
9.	–4.4	17.964	18.529

Thermodynamic properties of 3H4NB at different temperatures calculated by LSDA/6-311++G(d,p) method.

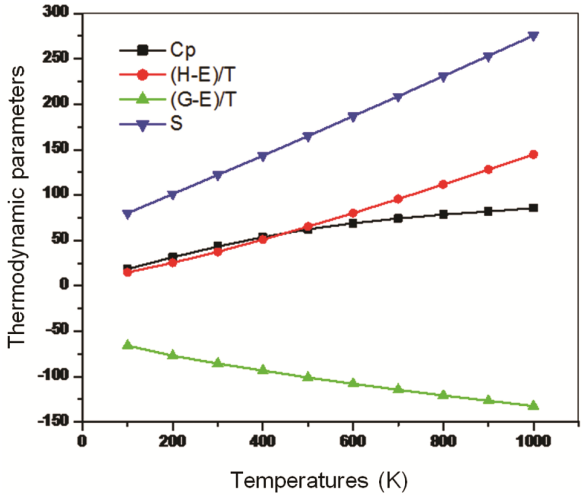

Fig. 16 — Thermodynamic parameters plot of 3H4NB.

Table 14 — Thermodynamic properties of 3H4NB at different temperatures calculated by LSDA/6-311++G(d,p) method.

Temp (K)	CP (calmol^{-1}K^{-1})	(H-E)/T (kcalmol^{-1})	(G-E)/T (kcalmol^{-1})	S (kcalmol^{-1})
100	27.627	24.916	–75.934	89.939
200	41.436	35.435	–86.897	111.232
300	53.219	47.587	–95.636	132.113
400	63.713	60.913	–103.414	153.316
500	72.275	75.133	–110.869	174.892
600	78.997	89.966	–117.813	196.768
700	84.289	105.579	–124.389	218.858
800	88.494	121.569	–130.629	240.988
900	91.899	137.954	–136.448	263.391
1000	95.435	154.667	–142.199	285.756

Table 15 — The calculated thermodynamics and molecular parameters are for 3H4NB.

Parameters	LSDA/6-311++G(d,p) level of theory
Self-consistent field energy (a.u)	–3004.793
Zero-point vibrational energy (Joules/mol)	295345.7
Zero-point vibrational energy (Kcal/mol)	71.788
Rotational temperatures (Kelvin)	
A	0.089
B	0.034
C	0.025
Rotational constants (GHZ)	
A	1.856
B	0.672
C	0.484
Thermal energy (E) (kcal/mol)	
Translational	0.898
Rotational	0.897
Vibrational	75.456
Molar capacity at constant volume (cal/mol k)	
Translational	2.993
Rotational	2.984
Vibrational	30.459
Entropy total (cal/mol k)	
Translational	41.847
Rotational	30.657
Vibrational	28.814
Thermal properties (Hartree/particle)	
Zero-point correction	0.115
Thermal correction to Energy	0.127
Thermal correction to Enthalpy	0.126
Thermal correction to Gibbs Free Energy	0.078
Sum of electronic and zero-point Energies	–3003.681
Sum of electronic and thermal Energies	–3003.673
Sum of electronic and thermal Enthalpies	–3003.669
Sum of electronic and thermal Free Energies	–3003.723
Dipole moment (Debye)	2.6014

$$Cp=3.435+0.312T-0.009T^{2}\left(R^{2}=0.999\right) \ldots (14)$$

$$\left(H-E\right)/T=0.587+0.265T-0.005T^{2}\left(R^{2}=0.999\right) \ldots (15)$$

$$\left(G-E\right)/T=-66.69-0.138T-0.009T^{2}\left(R^{2}=0.999\right) \ldots. (16)$$

$$S=59.18+0.294T-0.007T^{2}\left(R^{2}=1.000\right) \ldots (17)$$

The equations and correlation graphs from Fig. 16 are given here for ease of reference. 3H4NB's thermodynamic data is critical for future studies. Due to the fact that they were done in the gas phase, none of these calculations apply to the solution. A comprehensive set of thermal molecular data is essential for further study of the subject molecule in the future. It is possible to calculate various thermodynamic aspects using the second law of thermodynamics and the thermodynamical calculation of chemical process parameters and directions.

16 Conclusion

The geometrical properties of the optimal structure for the 3H4NB molecule were calculated using quantum chemistry techniques in the current approach. FT-IR and FT-Raman spectral analyses revealed the presence of many vibrational modes in the compound's functional groups. A UV-Vis research found that the compound had strong optical transmittance in the visible range and a lower cutoff wavelength at 600 nm. Hirshfeld surface analysis reveals the strongest interactions to be O...H. Hydrogen bonding has a significant effect on microscopic nonlinearity. Noncen trosymmetric crystallisation enhances the SHG efficiency of the specimen. The charge distribution over the atoms can be determined via Mulliken charge transfer. In light of these findings, it appears that the aforementioned chemical is suitable for usage in NLO applications. The 3H4NB molecule has a HOMO–LUMO energy gap, which confirms that the charge transfer is taking place. The computational and experimental results for proton and 13C NMR chemical shift were compared to ppm, and excellent agreement was found for both signals. This demonstrates that the regions of positive potential sites are located over electronegative oxygen atoms and around hydrogen atoms in the solid surface map, which was created using the Mapping electrostatic counter and solid surface map.

References

1 Vidal J P, Kirk-Othmer Encyclopedia of Chemical Technology, Wiley Online Library, 2006.

2 Yang L, Feng F & Gao Y, *Zhongguo Zhong Yao Za Zhi*, 34 (2009) 1805.
3 Xu J, Tan N, Zeng G, Han H, Huang H, Ji C, Zhu M & Zhang Y, *Zhongguo Zhong Yao Za Zhi*, 34 (2009) 990.
4 Chen W, Tang S, Qin N, Zhai H & Duan H, *Zhongguo Zhong Yao Za Zhi*, 37 (2012) 806.
5 Khaliq-uz-Zaman S M, Simin K & Ahmad V U, *Fitoterapia J*, 71 (2000) 331.
6 Lee K, Park S K, Kwon B M, Kim K, Yu H E, Ryn J, Oh S J, Lee K S, Kang J S, Lee CW, Kwon M G & Kim H M, *Xenobiotica J*, 29 (2009) 881.
7 Panoutsopoulos G I & Beedham C, *Pharmacol J*, 73 (2005) 199.
8 Dodd-O J M & Pearse D B, *Am J Physiol*, 279 (2000) 303.
9 Frisch M J et. al., Gaussion 09W Program, Gaussian, Inc, Wallingford, CT, 2004.
10 Dennington R D, Keith T A & Millam, J M, Gauss View5.0.8, Gaussian Inc, Wallingford, 2016.
11 Sundius T, *Vib Spectrosc*, 29 (2002) 89.
12 Ditchfleld R, *J Chem Phys*, 56 (1972) 5688.
13 Glendening E D, Badenhoop J K & Reed A E, Carpenter J E, Bohmann J A & Morales C M, NBO 5.0 Program, Theoretical Chemistry Institute, University of Wisconsin, Madison, 2001.
14 König F B, Schönbohm J & Bayles D, *J Comput Chem*, 22 (2001) 545.
15 Lu T & Chen F, *J Comput Chem*, 33 (2012) 580.
16 Morris G M, Huey R, Lindstrom W, Sanner M F, Belew R K, Goodsell D S & Olson A J, *J Comput Chem*, 30 (2009) 2785.
17 Rizal M R, Azizul I & Weng Ng S, *Acta crystallographica E*, 2008, DOI: 10.1107/S1600536808011148.
18 Sebastian S & Sundaraganesan N, *Spectrochim Acta Part A*, 75 (2010) 941.
19 Michalska D, Bieńko D C, Abkowicz-Bieńko A J & Latajka Z, *J Phys Chem*, 100 (1996) 17786.
20 Varsányi G, Lang L & Mikhail A K, Assignments for Vibrational Spectra of Seven Hundred Benzene Derivatives, Academic Kiado, Budapest, 1 (1973).
21 Stuart B H, Infrared Spectroscopy: Fundamentals and Applications, John Wiley & Sons, England, (2004).
22 Unal A & Eren B, *Spectrochim. Acta part A*, 114 (2013) 129.
23 Mohan J, Organic Spectroscopy, Principles and Applications, 2nd Edn, New Age International (p) Limited Publishers, New Delhi, (2001).
24 Parimala K & Manimegalai S, *Mater Today Proc*, 60 (2022) 1575.
25 Kalsi P S, Spectroscopy of Organic Compounds, 6th Edn, New Age International (p) Limited Publishers, New Delhi, (2004).
26 Parimala K & Manimegalai S, *Mater Today Proc*, 59 (2022) 636.
27 Silverstein M, Clayton Bassler G & Morrill C, Spectrometric Identification of Organic Compounds, Wiley, New York, 1981.
28 Lin-Vien D, Colthup N B, Fateley W G & Grasselli J G, The Handbook of Infrared and Raman Characteristic Frequencies of Organic Molecules, Academic Press, Boston, MA, 1991.
29 Sundaraganesan N, Meganathan C, Domnic Joshua B, Mani P & Jayaprakash A, *Spectrochim. Acta Part A*, 71 (2008) 1134.
30 George S, Infrared, Raman Characteristics Group Frequencies, Tables and Charts, 3rd Edn, Wiley, Chichester, 2001.
31 Parimala K & Manimegalai S, *Indian J Pure Appl Phys*, 60 (2022) 49.
32 Kanna R R A & Syam S N, *Spectrochim. Acta Part A*, 49 (1993) 1691.
33 Kurtz S K & Perry T T, *J Appl Phys*, 39 (1968) 3798.
34 Zyss J & Oudar J L, *Phys Rew A*, 26 (1982) 2028.
35 Anthony G, Rui F S & Marvin W, *Phys Today*, 47 (1994) 51.
36 Weinhold F, Landis C R & Glendening E D, *Int Rev Phys Chem*, 35 (2016) 399.
37 Agwupuye J A, Neji P A, Louis H, Odey J O, Unimuke T O, Bisiong E A & Ntui T N, *Heliyon*, 7 (2021) e07544.
38 Enudi O C, Louis H, Edim M M, Agwupuye J A, Ekpen F O, Bisong E A & Utsu P M. *Heliyon*, 7 (2021) e07531.
39 Gladis Anitha E, Joseph Vedhagiri S & Parimala K, *Spectrochim Acta Part A*, 136 (2015) 1557.
40 Fukui K, Theory of Orientation and Stereoselection, first edit, Springer-Verlag, Berlin, 1975.
41 Gnanasoundar I D, Joseph V S, Govindarajan M & Parimala K, *Mater Today: Proc*, 60 (2022) 1712.
42 Fleming J, Frontier Orbitals and Organic Chemical Reactions, John Wiley, London, 1976.
43 Mulliken R S, *J Am Chem Soc*, 74 (1952) 811.
44 Yang W & Parr R G, *Proc Natl Acad Sci*, USA 82 (1985) 6723.
45 Parr Y R G, Functional Theory of Atoms and Molecules, Oxford University Press, New York, 1989.
46 Ayers P W & Parr R G J, *Am Chem Soc*, 122 (2000) 2010.
47 Parr R G & Yang W J, *Am Chem Soc*, 106 (1984) 4048.
48 Morell C & Grand A, *J Phys Chem*, A 109 (2005) 205.
49 Johnson E R, Keinan S, Mori-Sanchez P, Contreras-Garcia J, Cohen A J & Yang W, *J Am Chem Soc*, 132 (2010) 6498.
50 Lu T & Chen F, *J Comp Chem*, 33 (2012) 580.
51 Humphrey W, Dalke A & Schulten K, *J Mol Graph*, 14 (1996) 33.
52 Glide, Schrödinger L L C, New York, NY, USA, Ver. 6 (2013) 1.
53 Maruthanila V L, Elancheran R, Roy N K, Bhattacharya A, Kunnumakkara A B, Kabilan S & Kotoky J, *Curr Comput Aided Drug Des*, 15 (1) (2019) 89.